CrossMark

Investigation of Gravity-Driven Drainage and Forced Convective Drying in a Macroporous Medium Using Neutron Radiography

Sreeyuth Lal[1,2,3] · **Lily D. Poulikakos**[4] · **Iwan Jerjen**[5] · **Peter Vontobel**[6] · **Manfred N. Partl**[4] · **Dominique Derome**[1] · **Jan Carmeliet**[1,7]

Abstract The co-occurrence of gravity-driven drainage and forced convective drying in a macroporous medium is investigated in this study. The drainage and drying processes of fully saturated porous asphalt (PA) specimens placed in a custom-made mini wind tunnel are documented with neutron radiography (NR). Six PA specimens of dimensions $180 \times 10 \times 30 \, \text{mm}^3$ with a maximum aggregate size of 8 or 11 mm are used in the experiments. In the first few minutes of each experiment, there is significant moisture loss in all the specimens due to gravity-driven drainage. Most of the residual water retention is observed at the bottom region of the specimens due to the strong impact of gravity-driven drainage in the upper regions. The specimens are subjected to many hours of airflow at their top surface; however, forced convection from turbulent airflow near the upper part of the specimens is found to have a minor influence on moisture loss when there are no water clusters in the upper regions of the specimens. This points to the strong resistance to evaporation in PA as a result of the large vapor diffusion lengths. By combining neutron radiography and microcomputer tomography (X-ray μ-CT) images, saturated and unsaturated flows in the pores are distinguished. Fluid

✉ Sreeyuth Lal
  sreeyuth.lal@psi.ch

[1] Laboratory for Multiscale Studies in Building Physics, Empa, Swiss Federal Laboratories for Materials Science and Technology, Uberlandstrasse 129, 8600 Dübendorf, Switzerland

[2] Department of Civil, Environmental and Geomatic Engineering, ETH Zurich, 8093 Zurich, Switzerland

[3] Electrochemistry laboratory, Paul Scherrer Institute, 5232 Villigen PSI, Switzerland

[4] Road Engineering/Sealing Components Laboratory, Empa, Swiss Federal Laboratories for Materials Science and Technology, Uberlandstrasse 129, 8600 Dübendorf, Switzerland

[5] Laboratory for Electronics/Metrology/Reliability, Empa, Swiss Federal Laboratories for Materials Science and Technology, Uberlandstrasse 129, 8600 Dübendorf, Switzerland

[6] Laboratory for Neutron Scattering and Imaging, Paul Scherrer Institute, 5232 Villigen PSI, Switzerland

[7] Chair of Building Physics, ETH Zurich, 8093 Zurich, Switzerland

flow path during air entry and water redistribution is further analyzed by reconstructing the real three-dimensional pore geometry of the specimens from X-ray μ-CT scans.

1 Introduction

Drainage and evaporation are important transport phenomena in many porous materials that are exposed to the environment. Additionally, engineering applications like enhanced oil recovery (Fenwick and Blunt 1998), evapotranspirative cover systems for waste containment and mining sites (Cui and Zornberg 2008) and water management in polymer electrolyte membrane fuel cells (Gostick et al. 2007) also involve the study of multiphase flow within porous media. Evaporation of water from porous media is a coupled heat and mass transfer process driven mainly by atmospheric conditions as well as the hydraulic conductance and vapor diffusivity of the material. Early experimental investigations of heat transfer (Vafai et al. 1985; Amiri et al. 1995) and mass transfer (van Genuchten and Wierenga 1977; Geller and Hunt 1993) in microporous media gave many insights into the transport phenomena present at both the Darcy and non-Darcy scales. Forced convective heat and mass transfers have also been studied for different porosity scales, ranging from microporous media (James et al. 2010) to highly porous macroporous media (Calmidi and Mahajan 2000) to variable-porosity media (Vafai 1984). In case of a porous medium with pore sizes <1 mm undergoing drying in typical natural air flow conditions (mean wind speed < 4 m/s), Haghighi et al. (2013) concluded that considering only diffusion from individual pores across a constant boundary layer accounts for most of the evaporation predicted by the full advection-diffusion equation. However, the relative contributions of diffusion and advection to the total moisture loss from a porous medium that is dominated by pore sizes larger than 1 mm have not been explored yet.

Gravity-driven drainage in porous media is dependent on material characteristics such as wettability, pore size distribution, tortuosity and connectivity, which ultimately determine the contribution of gravity-driven drainage to the total moisture loss. Gravity-driven drainage (Prazak et al. 1992; Grattoni et al. 2001; Poulikakos et al. 2013b) and forced convective drying (Kuznetsov and Nield 2006; Alvarez and Flick 2007) in macro porous media have been studied separately, and only a few studies analyzed the co-occurrence of drainage and evaporation in porous media. Yang and Yanful (2002) studied evaporation and drainage, as a function of water level, in sand particles of different sizes. They observed that the coarse sand ($D_{10} = 0.9$ mm) lost water by both drainage and evaporation, while the fine sand ($D_{10} = 0.16$ mm) did not exhibit any drainage. Furthermore, they also observed that drainage in the coarse sand was not affected by evaporation. Although a desk fan was used to speed up evaporation, the wind speed is neither recorded nor considered as a parameter in their analyses. To the best of our knowledge, no detailed experimental study till date has investigated the combined effect of drainage and forced convective evaporation on the overall moisture loss in macroporous media.

In this study, we investigate gravity-driven drainage and forced convective drying from fully saturated porous asphalt (PA) specimens. Porous asphalt is a composite material used as the surface layer of roads to allow the seepage of water and thereby prevent aquaplaning and splash–spray effects during and after rain events. The acoustic absorption property of
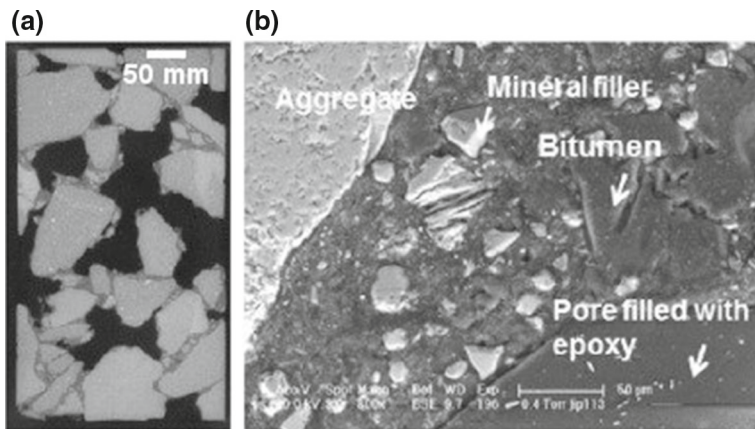
Fig. 1 Microstructure of porous asphalt concrete consisting of coarse and fine mineral aggregates, bitumen and air voids: **a** X-ray microtomographic slice of the specimen, where voids are *black*, aggregates *light gray* and bitumen *darker gray*, and **b** ESEM micrograph, the voids are filled with epoxy resin (*scale bar* 50 μm) [Figure adapted from Poulikakos et al. (2013a)]

PA leads to a significant reduction of vehicle tire noises on highways (Watts et al. 1999). The good hygric and acoustic properties are used to promote PA as an environment-friendly road material. PA typically has a porosity of around 20% and is a composite material made from fine and coarse mineral aggregates, a bituminous binder and air voids. In some cases, fibers are also added to PA to allow thick binder films for the sake of improved mechanical behavior and reduced binder drain-down effects. The microstructure analysis of PA (Fig. 1) shows the components in a typical PA internal structure. Ideally, the bituminous binder covers all particles with a thin hydrophobic layer. A description of a typical microstructure of PA is given in Poulikakos and Partl (2010).

There is considerable exposure of the internal structure of PA to water due to its high water permeability. Similar to field soils (Hillel 1971), evaporation and drainage co-occur in PA, where the time-scale of drainage is usually shorter. Hence, PA is more susceptible to moisture-induced deterioration than dense asphalt concrete, resulting in a shorter service life (Partl et al. 2008). Water induces deterioration in PA primarily by affecting binder cohesion and the adhesion between binders and aggregates, a process known as stripping (Poulikakos and Partl 2012). Therefore, from the point of view of durability, it is important to analyze the residence time of water in PA under different wetting and drying conditions. Using neutron radiography (NR) imaging, Lal et al. (2014) studied wetting in PA with a water uptake experiment, while Poulikakos et al. (2013b) studied water drainage from PA. Poulikakos et al. (2013a) studied evaporation of water from PA after blocking drainage. The complexity of water redistribution in PA was evident in all these experiments. Indeed, Yang and Yanful (2002) observed that evaporation in porous media is significantly affected by water redistribution. As opposed to the aforementioned papers, in this study, the co-occurrence of drainage and evaporation of water from PA is analyzed in detail. Additionally, the PA specimen size ($28 \times 47 \times 10$ mm^3) in Poulikakos et al. (2013a), Poulikakos et al. (2013b) and Lal et al. (2014) was too small to draw any general conclusions about drying of PA. Given that the focus of their study was to analyze the macroscopic moisture profiles as well as to visualize the spatial and temporal distributions of moisture, a detailed investigation into the physics of water transport in such conditions was not undertaken in their work.

In light of the studies mentioned above, the objectives of this study are twofold: to estimate the overall moisture loss from fully saturated PA specimens due to the co-occurrence of gravity-driven drainage and forced convective drying and to understand the mechanisms by which water leaves the specimen and is redistributed within the specimen due to capillary effect and gravity. We use neutron radiography (NR) imaging to obtain the spatial and temporal distributions of moisture content in PA during the drainage and drying stages. By combining NR images with pore structure information obtained from microcomputer tomography (X-ray μ-CT) scans, we can clearly distinguish between saturated and unsaturated flows within the PA structure. In addition, by reconstructing the real 3D PA geometry from X-ray μ-CT scans, we also visualize the flow path of water within the specimen during certain events.

As will be shown later in this study, the drainage and drying behaviors of PA is very different to that of conventional porous media. Though there have been many studies which observe and model drainage and drying in porous media with well-defined evaporation and percolation fronts (e.g. Bergstad and Shokri 2016; Hoogland et al. 2016; Shokri et al. 2012; Teng et al. 2016), the exploration of cluster-based drying behavior, which is what we observe in our experiments, is hardly given any attention in literature. Our findings can be used to provide more accurate boundary conditions for drying models that focus on cluster-based drying in porous media (Moghaddam et al. 2017). Due to its pore sizes in the millimeter-centimeter range, fluid transport in PA is comparable to that in a fractured medium and consequently, the results of this study will be of interest in areas such as oil extraction in fractured reservoirs. Furthermore, optimizing the microstructure of PA for the maximum hydraulic conductivity is an ongoing process (Aboufoul and Garcia 2017), for which a thorough knowledge of liquid transport in PA is required.

In the next section, first the characteristics of the specimens investigated in this study are detailed, followed by a brief description of the imaging techniques used and the details of the experimental procedure. We then present the results, discuss them in detail, list future avenues of research and finally present our conclusions.

2 Materials and Methods

2.1 Material Description

The two porous asphalt materials used in this study, PA8 and PA11, are obtained directly from a local mixing plant. They satisfy Swiss standards and contain 6 mass% polymer-modified bitumen, PmB-E 45/80-65, and 0.2 mass% cellulose fibers. PA8 has a maximum aggregate size of 8 mm whereas PA11 has a maximum aggregate size of 11 mm. Specimens with dimensions $180 \times 500 \times 50\,mm^3$ and an approximate mass of 18 kg are compacted at 155 °C in the laboratory using a rolling compactor. Thereafter, the bottom 20 mm is cut away and the final specimens are cut to dimensions of $180 \times 10 \times 30\,mm^3$. The top surface of the specimen is rough, replicating field conditions. In this study, three PA8 and three PA11 specimens are investigated. The specimens are named PA8(A), PA8(B), PA8(C), PA11(A), PA11(B) and PA11(C). During the experiments, specimens PA8(A) and PA11(A) are taped at the bottom $x - z$ plane (Fig. 2) with an aluminum tape to constrain gravity-driven drainage. This configuration replicates best the physical processes occurring in situ where the interface to the next asphalt layer is sealed and as a result, the drainage occurs sideways. All the other four specimens are open on all sides. Since all the specimens used in this study are
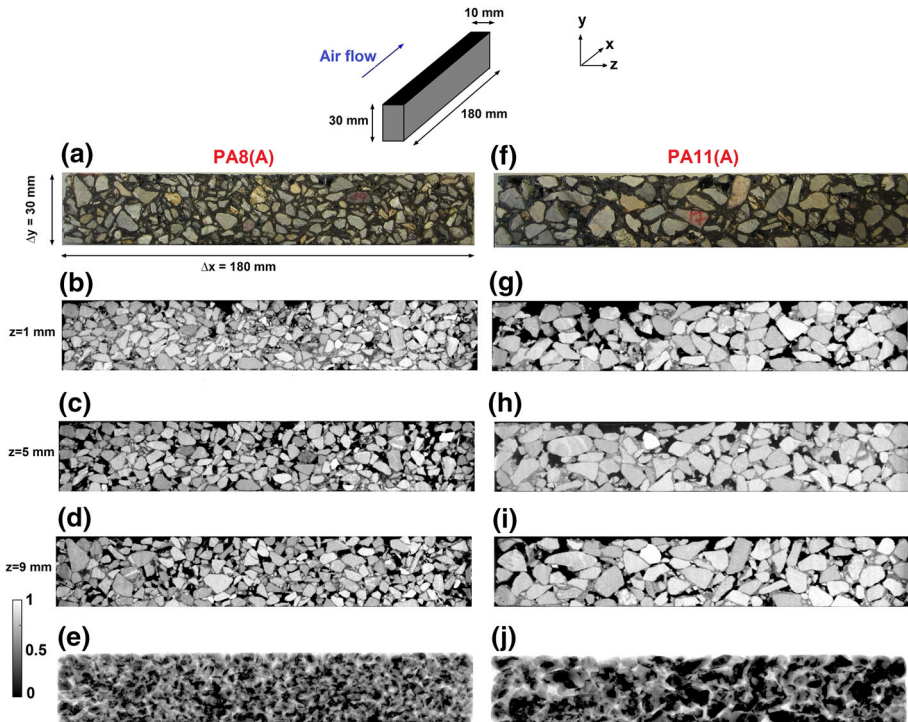
Fig. 2 Schematic depiction of the specimen (*top*). Visible light photographs (**a**, **f**), X-ray microtomographic slices of the x–y planes at $z = 1$ mm (**b**, **g**), $z = 5$ mm (**c**, **h**), $z = 9$ mm (**d**, **i**) and 2D cumulative porosity distribution images (**e**, **j**), in which the porosity ranges from 0 (*black*) to 1 (*white*), of PA8(A) and PA11(A) specimens

freshly-prepared, the solid matrix of the specimens is expected to be hydrophobic, since the binder-water contact angle for a similar binder is measured to be 92° (Poulikakos and Partl 2012).

2.2 Material Characterization

The pore structures of the specimens are imaged with an X-ray micro-computed tomography (X-ray μ-CT) setup. The X-ray μ-CT instrument is custom-made using commercial components: an X-ray tube (XT9225-TEP from Viscom), a flat panel X-ray detector (XRD 1621 CN3 ES from PerkinElmer, 200 μm pixel size) and a high precision rotation stage (UPR-160 F air from Micos) mounted on three linear stages (LS-270 from Micos). All components are installed on an optical-table with a passive vibration dampening mechanism (Type HDT with a DMT base frame from Opta). The specimens are mounted together at a distance of 503.2 mm from the X-ray source and at a distance of 467 mm from the detector. From a pixel size of 200 μm and a geometrical magnification of ~1.9, a spatial resolution of 103.7 μm is obtained in the final 3D dataset. The chosen tube parameters are an acceleration voltage of 200 kV and a nominal current of 100 μA. In order to reduce artifacts, the X-ray spectrum is hardened by means of a 1 mm Cu filter. For each scan, a region of interest of 1000×2000 pixels is chosen given the elongated geometry of the objects. Seven hundred and twenty radiographic images are recorded with a total integration time of 10 s per image from differ-

ent viewing angles distributed over 360° in 0.5° steps. The X-ray detector is calibrated before the start of the measurement, and no additional dark and flat field corrections are necessary. After ring and beam hardening artifact corrections, the three-dimensional spatial distribution of the attenuation coefficient is calculated by a self-written Feldkamp code (Feldkamp et al. 1984). For the overlapping of the X-ray μ-CT images with the neutron radiography images as described in Sect. 3.2, the spatial resolution of the X-ray μ-CT images is reduced to 150 μm by bilinear interpolation.

In Fig. 2, visible light photographs (a, f), X-ray μ-CT slices at $z = 1$ mm (b, g), $z = 5$ mm (c, h), and $z = 9$ mm (d, i), and the two-dimensional cumulative porosity distributions (CPD) obtained from reconstructions of 3D X-ray μ-CT scans (e, j), are shown for one specimen each from the PA8 and PA11 types of material. In the CPD figures, the blackest regions represent the presence of an aggregate along the entire thickness (z-direction) of the specimen, i.e., the porosity is 0. In contrast, the whitest regions represent the presence of a pore space along the entire thickness of the specimen, i.e., the porosity is 1. Intermediate gray values represent porosities between 0 and 1 along the specimen thickness. The procedure to calculate 2D CPD from 3D scans is described in detail in Lal et al. (2014). The CPD figures are later used for calculating the degree of saturation of liquid in the specimens.

In Figs. 3 and 4, the pore size and throat length distributions of the six specimens used in this study are given, as estimated by the Maximal Ball algorithm (Dong and Blunt 2009). The maximal ball (MB) algorithm works by fitting the largest possible spheres, centered on each air voxel, such that they just touch the solid boundary. Spheres that are completely inscribed within other spheres are removed and the remaining spheres are called maximal balls, where the largest maximal balls are considered as pores and the smaller balls between them are considered as throats. From Figs. 3 and 4, it can be seen that the pore size and throat length distributions of all the PA8 and PA11 specimens used in this study are largely similar, although PA11 specimens in general are expected to have larger pores. However, due to small thickness of the specimens in this study, a few of the large pores,
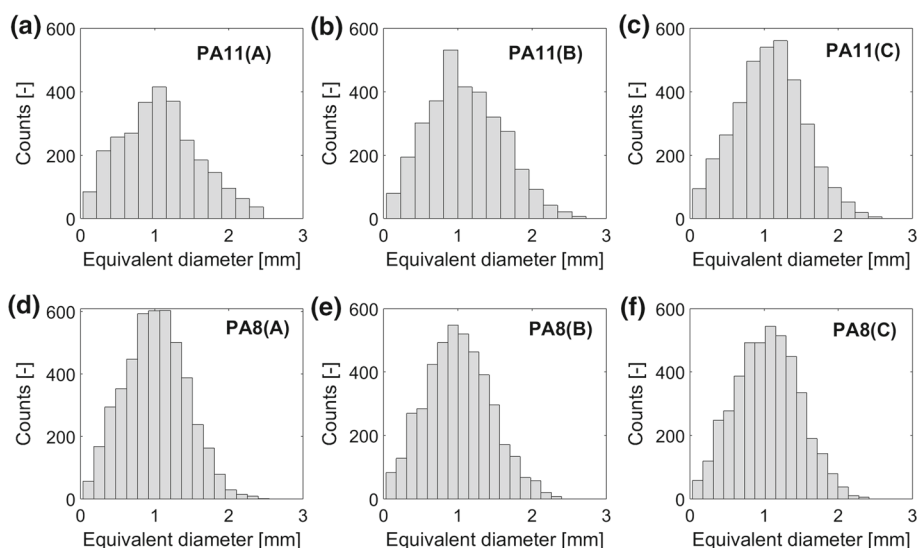
Fig. 3 Pore size distribution of the six PA specimens used in this study, estimated with the Maximal Ball algorithm
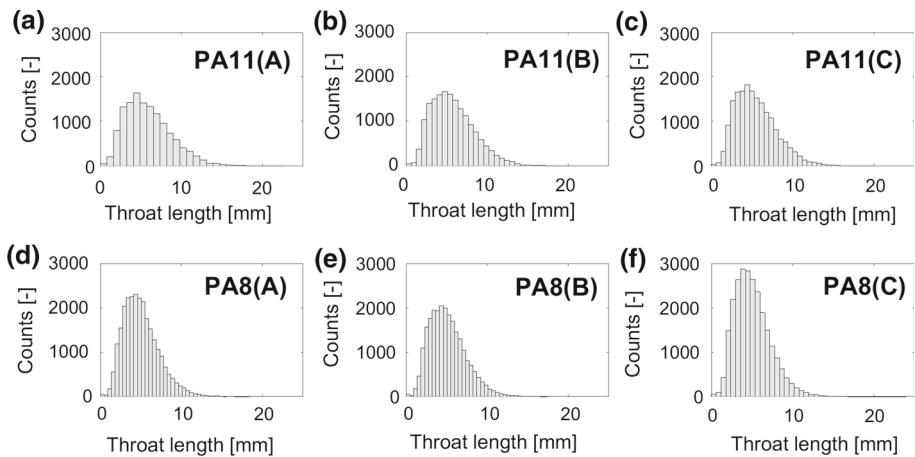
Fig. 4 Throat length distribution of the six PA specimens used in this study, estimated with the Maximal Ball algorithm

especially in PA11, will not be fully captured. Therefore, we note that the specimen thickness of 10 mm is not a representative thickness of an actual PA pavement (Lal et al. 2014), but the available neutron beam does not have the energy to go through thicker specimens. However, the specimen dimensions in the other two directions (x, y) are good representations of an actual pavement since a representative dimension should be 2.5 to 3 times larger than the maximum aggregate size (8 and 11 mm in the current specimens). Moreover, the presence of pores larger than 2 mm in all the specimens clearly make the specimens macroporous.

2.3 Experimental Setup and Procedure

2.3.1 Neutron Radiography

The experiments were performed at the NEUtron Transmission RAdiography (NEUTRA http://www.psi.ch/sinq/neutra/) beam line of the Paul Scherrer Institute (PSI) in Villigen, Switzerland. The source of the neutron beam is the Swiss Neutron Spallation Source (SINQ), which provides a neutron beam with a thermal energy spectrum, i.e., neutrons with a most probable energy of 0.025 eV and a speed of 2200 m/s. Neutrons within the thermal energy spectrum have a high interaction probability with hydrogen, making the NEUTRA beamline appropriate for tracking the flow of water inside porous materials. The features of this facility include high collimation ratio, low gamma background and large beam diameter. A detailed description of the entire setup is given by Lehmann et al. (2001). The imaging detector consists of a 100 µm thick ^{6}Li doped zinc sulfide scintillator screen and a CCD camera. We used a Andor iKon-L camera with 2048×2048 pixels with a region of interest setting of 1370×1010 pixels, providing a field of view of 206×152 mm^2. The exposure time in the experiments was 23 s per radiograph with an attained spatial resolution of 150 µm per pixel. The neutron chamber had a temperature of approximately 26 °C and 40% relative humidity during these experiments.
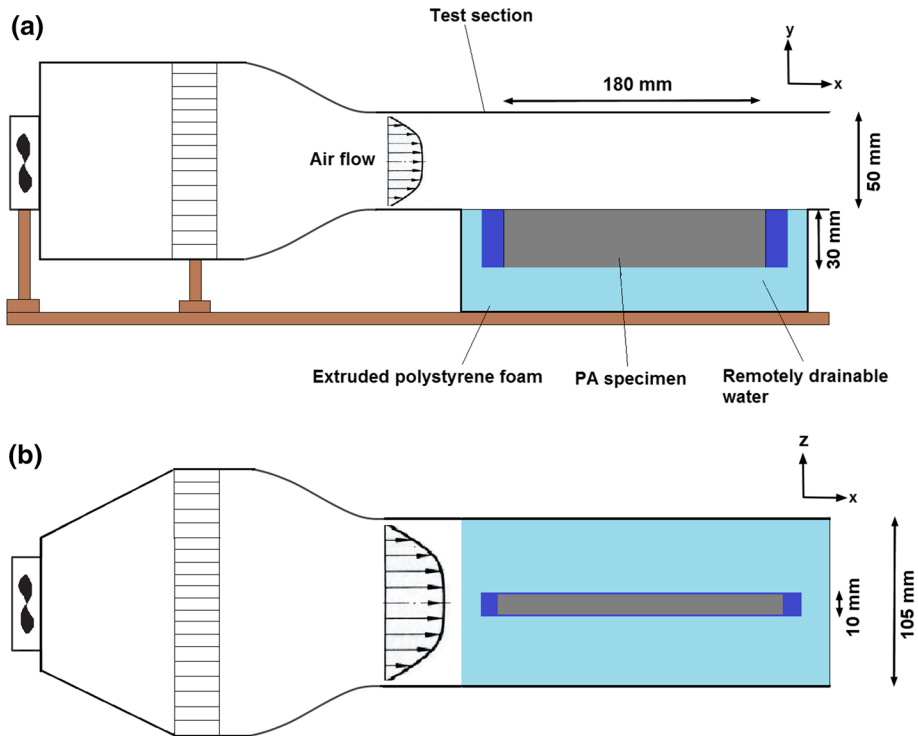
Fig. 5 Schematic representation of the mini wind tunnel. **a** Side view and **b** top view

2.3.2 Mini Wind Tunnel

A custom-made mini wind tunnel was used for the experiments, and the schematic of which is shown in Fig. 5. The airflow generated by the fan first passes through a two-dimensional diffuser with an expansion ratio of 1.5. Thereafter, the air passes through screens and honeycomb in order to minimize the turbulence and swirl generated from the fan. The airflow is then directed to the test section by a three-dimensional contraction with a contraction ratio of 2. The test section, where the PA specimen is placed during the experiments, is 50 mm high and 105 mm wide. A part of the sidewalls of the test section is made of pure aluminum to minimize neutron absorption and scattering in the region of interest. The test section of the wind tunnel is designed to be drained remotely. Once drainage is activated remotely, water flows out from the test section via a tube that is connected to the base of the test section (not shown in figure). The specimens are surrounded by extruded polystyrene foam (Styrofoam) in the test section, which acts as a thermal insulator. Due to the extremely low water absorption (0.3% by volume after 24 h of immersion in water as per the ASTM C272 test) and water vapor permeance (57.2 ng/Pa.s.m^2 as per the ASTM E96 test) of Styrofoam, the drainage and drying process in PA is not expected to be influenced by the surrounding foam. The wind tunnel is fitted with temperature and relative humidity sensors to gather information about the neutron chamber environment. During the experiments, the fan is operated at a voltage of 8 V, which translates to a mean wind speed of approximately 1.5 m/s, as measured by a hot-wire anemometer ($\pm 2\%$ accuracy) at the outlet of the test section. At this speed, the calculated Reynolds number at the test section, using the height of the

channel as the representative length, is $Re = 6500$, clearly indicating turbulent flow in the channel.

2.3.3 Drainage and Drying Experiments

The drainage and drying behavior of three PA8 and three PA11 specimens from a fully saturated state are documented in this study. The specimens are first submerged in deionized water for at least 8 h. Previous laboratory tests have shown that this is a sufficient time for the specimen to be fully saturated with water. At the beginning of each experimental run, a specimen is taken out of water, its sides are wiped with a cloth to ensure that there is no water dripping out and the mass of the specimen is recorded on a microbalance. The specimen is then placed in the test section of the mini wind tunnel, and the test section is flooded with deionized water. Once the neutron beam is activated and the first two images are acquired, the water in the test section is drained remotely, and neutron radiographs are acquired every 30 s. This remote draining procedure makes it possible to record the gravity-driven drainage in the PA specimens that occurs in the first few minutes. When most of the drainage is completed, i.e., after 60 or 120 min (depending on the experiment), the fan in the mini wind tunnel is switched on to initiate forced convective drying of the specimen. In this way, the impact of airflow on the total moisture loss from the specimen could be clearly identified. The total duration of the experimental runs varied from 6 to 11 h. At the end of each experimental run, the specimen is taken out of the test section and its mass is again recorded. The specimen is then dried inside a convection oven at 55 °C and its mass is monitored regularly. Once fully dry, a neutron image of the dry specimen is acquired as a reference image, allowing the quantification of moisture content (see next section). The mass measurements of the specimen taken at the different stages of its wetness are used as control values for the corrections of the water mass detected by neutron radiographs.

2.3.4 Derivation of Water Content from Neutron Radiography

The first step of postprocessing of the neutron radiographs is to correct them for different types of artifacts. The corrections performed on the NR images in this experiment, in the order of their application, are as follows:

1. Dark current correction: corrects the offset from thermally generated electrons in the charge-coupled device of the CCD camera.
2. Black body correction: corrects the signal from the neutrons that are scattered from the experimental setup or the environment to the detector.
3. Spectral effect correction: accounts for the shift in the mean neutron beam energy to higher energies after traversing a strongly attenuating specimen.
4. Intensity correction: scales the measured radiographs so that all the radiographs acquired in the experiment have equal neutron exposure.
5. Flat field correction: accounts for the spatial inhomogeneity of the neutron beam intensity and detector sensitivity.

The reference images required for the dark current, black body and flat field corrections are acquired during the experiments. For the mathematical representation of the image corrections, the reader is referred to Lal et al. (2014).

After applying all the corrections, the spatial and temporal distributions of moisture content are quantified from the NR images. Neutron radiography is based on neutron transmission measurements, which depend on material thickness and composition. Neutrons interact with

the atomic nucleus, especially hydrogen, and hydrogen bound in water shows a high neutron attenuation capacity due to scattering. The Beer–Lambert law for the attenuation of radiation passing through matter can be written as:

$$I = I_0 e^{-(\Sigma/\rho)\rho d}, \tag{1}$$

where $I[-]$ is the final beam intensity after the beam traverses a distance of $d[\text{m}]$ in the specimen, $I_0[-]$ is the incident beam intensity, $\rho[\text{kg m}^{-3}]$ is the mass density of the specimen, $\Sigma[\text{m}^{-1}]$ is the linear attenuation coefficient and the term (Σ/ρ) is the mass attenuation coefficient. From eq. (1), we can calculate the mass thickness, $\tau[\text{kg m}^{-2}]$ (Hassanein et al. 2005), i.e., the product of the specimen density and the specimen thickness at each pixel, as:

$$\tau(x, y) = \rho(x, y)d(x, y) = -\frac{\rho(x, y)}{\Sigma} \ln \frac{I(x, y)}{I_0(x, y)}, \tag{2}$$

where (x, y) denotes the coordinates of a pixel in the $x - y$ plane, i.e., normal to the neutron beam. In this study, the temporal evolution of moisture within the specimens is tracked with the parameter called as moisture content distribution (MCD), which is the mass of water per unit volume of the specimen. From the mass thickness, the MCD, $w_t[\text{kg m}^{-3}]$, can be calculated as:

$$w_t(x, y) = \frac{\tau(x, y)_t - \tau(x, y)_i}{d_z}, \tag{3}$$

where $d_z[\text{m}]$ is the constant specimen thickness in the direction of the beam (z-direction), $\tau(x, y)_t$ is the mass thickness of water at a given pixel at time t and $\tau(x, y)_i$ is the mass thickness of water at the same pixel in the dry specimen. Combining Eqs. (2) and (3), the MCD can be rewritten as:

$$w_t(x, y) = -\frac{\rho(x, y)}{\Sigma d_z} \ln \frac{I(x, y)_t}{I(x, y)_i} = -\frac{\rho(x, y)}{\Sigma d_z} [\ln I(x, y)_t - \ln I(x, y)_i], \tag{4}$$

where $I(x, y)_t$ and $I(x, y)_i$ are the beam intensity at a time t and the beam intensity of the dry specimen respectively, for a given pixel, as recorded by the detector after the beam traverses the entire thickness of the specimen. Since the presence of moisture within its internal structure does not cause any deformation in PA, no additional image registration for deformation is required and the moisture content at each pixel can be calculated by simply subtracting the logarithm of the dry image from the logarithm of the wet images.

3 Results and Discussion

3.1 General Observations

The aim of the experiments in this study is to understand how water exits from a porous asphalt layer after it is nearly saturated with water, for instance after a large rain event. Due to the wide range of pore sizes in PA, ranging from sub-microns to millimeters, a combination of different mechanisms such as gravity-driven drainage in the macropores, capillary-driven flow in the finer pores and evaporation is expected to occur simultaneously. In this section, moisture flow within the specimen is analyzed in detail to separate the different mechanisms from each other, and the conditions under which they occur are investigated. Figure 6 shows the temporal evolution of the average moisture content in the specimens (in kg/m^3). The time at which the fan is switched on for each of the specimens is indicated by an arrow on its
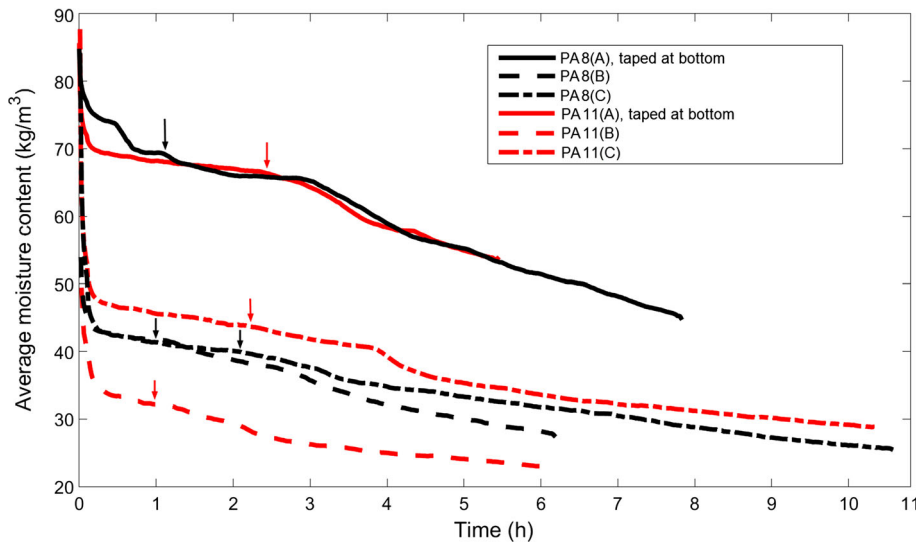
Fig. 6 Temporal evolution of average moisture content in the six specimens. *Arrows* indicate the time at which the fan was switched on. The fan continued to run until the end in all the experiments
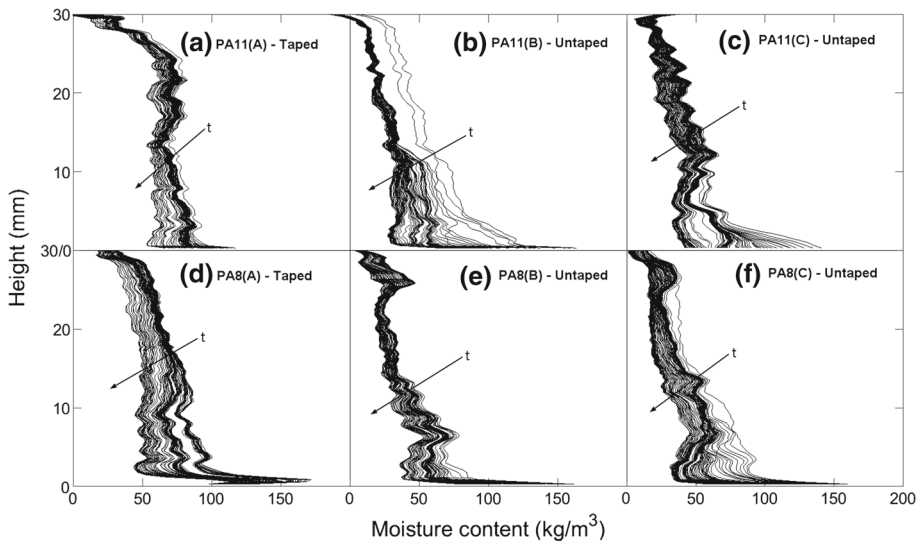
Fig. 7 Temporal evolution of moisture profiles in the six specimens. Profiles are shown for every 30 s for the first 15 min, every 2.5 min for the next 2 h and every 5 min for the remaining duration of the experiments

corresponding curve. We remind that images are taken every 30 s. Since the bulk of drainage in PA is an extremely fast process in the order of a few seconds, most of the water within the specimen is drained by the time the first image is obtained. Therefore, the first data points of the curves in Figs. 6, 7 and 8 have different values due to different moisture retention depending upon the specimen type and boundary conditions, although the initial condition at

$t = 0$ s is the same for all specimens, i.e., all specimens were fully saturated at the beginning of drainage.

The most apparent observation from Fig. 6 is the higher water retention by specimens PA8(A) and PA11(A), both of which are taped at the bottom and which, as mentioned earlier, is the closest to the real in situ situation. This high water retention occurs despite the fact that the sides of the specimens are open and gravity-driven drainage could have occurred through the sides as well. The other specimens show a high initial moisture loss, which shows the significance of the contribution of gravity-driven drainage from the bottom side toward the overall water loss from a specimen. It can also be observed that, except for specimens PA8(A) and PA11(A), switching on the fan does not increase the rate of moisture loss significantly. This points to the limited effect of drying by forced convection at a mean wind speed of 1.5 m/s. This observation is investigated again through Fig. 7. It is also seen from Fig. 6 that there are clear changes in the slopes of the curves during drying, e.g., at $t = 4$ h in PA11(C). A close analysis of the NR images shows that these 'bursts' of drying occur due to the drying of a large cluster of water that is connected to an open edge. It is unlikely that these bursts of drying are influenced by airflow since these water clusters occur at a depth little affected by the airflow above.

Furthermore, there is no significant difference between the drainage and drying behaviors of PA8 and PA11. This is due to the fact that the pore size distribution is only one of the factors influencing drainage and drying. Other factors such as pore connectivity and overall porosity are also important. As mentioned above, as the available neutron beam does not have the energy to go through very thick specimens, the specimen thickness in this study is restricted to 10 mm and, consequently, the behavior of these specimens will not be totally representative of PA at the pavement scale.

Moisture content profiles along the height of the specimens are given as a function of time in Fig. 7. In these images, for each selected time step, the moisture content is averaged over the entire length of the specimen (180 mm) for every 0.3 mm (2 pixels) along the specimen height, i.e., along the direction of gravity. The profiles are plotted for every 30 s for the first 15 mins, every 2.5 min for the next 2 h and every 5 min for the remaining duration of the experiment. In Fig. 7b, it can be seen that PA11(B) loses a lot of moisture in the first few times steps itself, which explains the steep drop of the average moisture content curve of PA11(B) in Fig. 6. In general, at the bottom part of the specimens, there is significantly higher moisture loss in the first few time steps, except in specimens PA11(A) and PA8(A), since they are taped. Thus, Fig. 7 gives a first indication of the importance of gravity-driven drainage, an aspect which will be explored in detail below. Another observation from Fig. 7 is that, in the case of the untaped specimens, the bottom part of the specimens shows a higher moisture content than the upper part even toward the end of the experiments. This higher moisture content at the bottom part can be attributed to the fact that gravity drains most of the water from the top due to the high static pressure head whereas some water is trapped in the pores at the bottom part due to the relatively lower static pressure head at the bottom. This entrapped water evaporates very slowly due to the large diffusion length within the specimen.

To analyze gravity-driven drainage as well as convective drying in more detail, the specimens are divided into different regions of interest (RoIs). The specimens are first divided vertically (along the direction of gravity) into three equal parts, namely RoIs 1, 2 and 3. RoI 1 is then divided horizontally into three equal parts, namely RoIs 4, 5 and 6, to analyze the effect of drying in sections along the direction of airflow. The RoIs are schematically depicted in Fig. 8. In Fig. 8a–f, the moisture loss from the RoIs as a fraction of the total moisture loss from the entire specimen is shown as a function of time. These figures are derived as follows: First, the total moisture loss from the entire specimen at a particular time step is
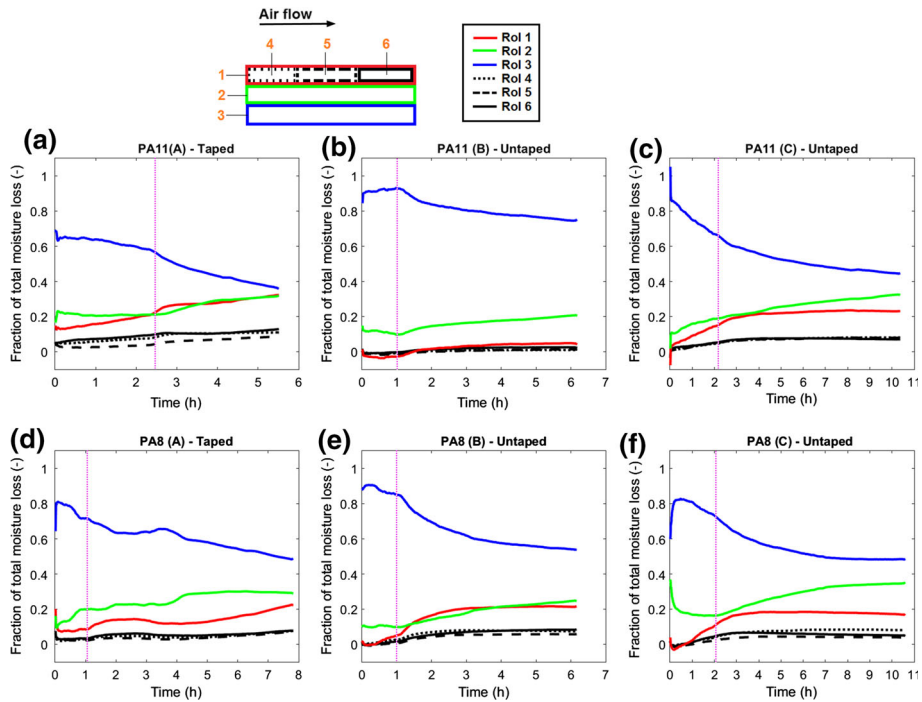
Fig. 8 Temporal evolution of the contribution of different regions of interest (RoIs) toward the total moisture loss in the specimen with schematic of the selected RoIs. The time at which the fan is switched on in each experiment is indicated by a magenta dotted line. The fan continued to run until the end in all the experiments

calculated by subtracting the image at that time step from the first wet image that is acquired immediately after the test section is allowed to start draining, i.e., at $t = 90$ s. Similarly, the moisture loss from all the other RoIs is calculated by restricting the image subtraction to only the respective RoIs. By dividing the moisture loss in each RoI at a particular time step with the total moisture loss in the entire specimen at the same time step, the contribution of each RoI toward the total moisture loss in the specimen at that time step can be determined. This process is repeated for all the time steps to obtain Fig. 8. The time at which the fan is switched in each experiment is indicated in the respective figure by a magenta dotted line.

Figure 8 offers an insight into the limited effect of convective drying in the untaped specimens, as was already observed from Fig. 6. After the fan is switched on, the drying rate of RoI 1, where the effect of convective drying will be the strongest as it is closest to the airflow, shows an immediate increase only in the two taped specimens, PA11(A) and PA8(A). This is due to the higher moisture retention at the top regions of the taped specimens as compared to the untaped specimens. Therefore, the limited effect of convective drying in the untaped specimens can be attributed to the long diffusion distance of water vapor from the lower region of the specimens. In the case of taped specimens, due to higher accumulation of water at the top regions, the diffusion length is smaller, and hence airflow influences drying to a certain extent. Furthermore, in all the specimens, RoI 3 is the region where most of the moisture loss occurs, although the mechanisms for this loss are different at the initial and final stages of the experiment. Due to the extremely strong effect of gravity, a significant fraction of the initial moisture content is lost when the first image is acquired after 30 s

from the remote activation of drainage. Thereafter, as reasoned before, the lower part of the specimen, RoI 3, retains most of the residual water due to the lower impact of gravity in this region. In the initial few time steps, RoI 3 also loses some moisture due to gravity. With time, evaporation and water vapor diffusion drives moisture loss instead of gravity. In this scenario, the contributions of RoIs 1 and 2 toward the total moisture loss show an increase as they are much closer to the top surface, and therefore, the vapor diffusion length is shorter for the water vapor generated from these regions, leading to faster evaporation. However, as RoI 3 always has a higher water content, and hence, a larger evaporating front, the contribution of RoI 3 toward the total moisture loss is always higher. Meanwhile, the time evolution of moisture loss in RoIs 4, 5 and 6 is quite similar. Studies of forced convective drying in microporous media have demonstrated the existence of a three-dimensional drying front which develops from the windward edge to the leeward edge and from the top surface (the surface exposed to air flow) to the bottom (Defraeye et al. 2012). However, RoI 4, the windward RoI, does not exhibit a higher rate of moisture loss as compared to RoIs 5 and 6.

3.2 Bond Number Analysis

To quantify the strong influence of gravity observed in the previous section, the Bond numbers of the specimens used in this study, Bo[−], are calculated and presented in Table 1. Although there are currently many definitions of the Bond number, which is essentially the ratio of gravity to capillary forces, we define Bo with pore space characteristics as length scales as (Hirsch and Thompson 1994):

$$\text{Bo} = \frac{\Delta \rho g l r}{2\gamma \cos \theta},$$ (5)

where $\Delta \rho [\text{kg m}^{-3}]$ is the density difference between air and water (998.8 kg/m^3 in this study), $l[\text{m}]$ is the characteristic throat length, $r[\text{m}]$ is the characteristic pore radius, $\gamma [\text{Nm}^{-1}]$ is the air-water surface tension at the experimental conditions (0.072 in this study) and $\theta[°]$ is the water-bitumen contact angle, which is 99.2° for the type of bitumen used in the specimens in this study (Poulikakos and Partl 2012). In Table 1, Bond numbers are calculated using both the average and maximum values of the pore radius and throat length as the characteristic values. The average and maximum pore radius and throat length of the specimens are estimated from their X-ray μ-CT scans using the Maximal Ball algorithm.

In Table 1, the average Bond number has values in the range 0.73–0.91 while the maximum Bond numbers have a significantly higher range, i.e., 6.15–8.23, which is an order of magnitude higher. The higher Bond number is a result of the high values of both the

Table 1 Stochastic Bond numbers of the specimens used in this study

Specimen	Pore radius, r (mm)		Throat length, l (mm)		Bond number, Bo (−)	
	Average	Maximum	Average	Maximum	Average	Maximum
PA11(A)	0.54	1.23	5.94	22.88	0.91	8.08
PA11(B)	0.55	1.36	5.79	20.92	0.91	8.17
PA11(C)	0.54	1.39	5.49	19.97	0.84	7.93
PA8(A)	0.50	1.27	5.04	18.85	0.73	6.87
PA8(B)	0.50	1.20	5.12	17.90	0.74	6.15
PA8(C)	0.52	1.21	5.07	23.78	0.76	8.23

maximum throat lengths and maximum pore radii, both of which lead to the dominance of gravity over capillary forces due to higher hydrostatic pressure and lower capillary force. Consequently, a huge difference between the average and maximum Bond number values points to the existence of a few well-connected, large pores, which are responsible for the bulk of the gravity-driven drainage in PA.

### 3.3 Analysis of Water Flow During a Sudden Drop in Moisture Content

In Fig. 6, it is observed that there is a sudden drop in moisture content inside the specimen PA8(A) around $t = 0.5$ h. From Fig. 8d, around the same time, we can observe a sudden rise in the contribution of RoI 2 toward the total moisture loss. This indicates that this sudden moisture loss occurs in the middle part of the specimen. We first track the temporal evolution of moisture content distribution (MCD) in the entire specimen, followed by focusing on a smaller region of interest where the sudden drop in moisture content takes place. The MCD plot of PA8(A) is given in Fig. 9a. A second series of images are shown in Fig. 9b to highlight areas undergoing considerable moisture loss. These images are derived using a procedure similar to the one used in Fig. 8, i.e., the moisture loss at a particular time step is calculated by subtracting the image at that time step from the first wet image at $t = 90$ s. In Fig. 9b, pixels have a binary representation, blue or white, where a white pixel is one whose value has crossed a moisture loss threshold of $30 \, \text{kg/m}^3$, while a blue pixel is one whose value does not change (e.g., absence of porosity) or whose moisture loss is below the threshold. This threshold has been selected to achieve a clear visualization of the spatial distribution of water by indicating only those areas in the specimen that undergo significant moisture loss.

Since PA8(A) was covered at the bottom with a tape, we can see that there is not a big difference between the MCD plots at $t = 0.07$ h and $t = 1.3$ h. Some moisture loss in the bottom corners, especially the left corner, can be visualized clearly in the thresholded image at $t = 1.3$ h. From this, it can be concluded that the sudden moisture loss observed in Fig. 6 is a result of water exiting from the bottom left corner. This will be analyzed in detail in the subsequent paragraphs. Complementary to the conclusion drawn from Fig. 8, no drying front can be seen in the windward to leeward direction at the top of the specimen. A strong bottom-up drainage front can be clearly observed, which continued long after the fan was switched on at $t = 1.2$ h. At $t = 7.8$ h, water-filled zones can be seen in a few regions of the specimen, demonstrating that the specimen still contains a lot of water even after more than 6.5 h of forced convective drying.

Our next objective is to understand the exact mechanism by which the sudden moisture loss in the bottom left corner of PA8(A) took place. For this purpose, a more detailed analysis of water redistribution is studied in terms of the degree of saturation (DoS), $s_t(x, y)[-]$, defined as:

$$s_t(x, y) = \frac{w_t(x, y)}{\rho_w \cdot \varphi(x, y)} \; , \tag{6}$$

where $\varphi(x, y)[-]$ is the two-dimensional porosity distribution as shown in Fig. 2, $w_t(x, y)$ is the MCD calculated with eq. (3) and ρ_w is the density of water. According to eq. (6), NR images should be divided by X-ray μ-CT images to get DoS images. However, the image resolutions of the NR and X-ray μ-CT images are different. Therefore, as mentioned above, using bilinear interpolation, the resolution of X-ray μ-CT images is lowered to match that of NR images before division. Unlike MCD analysis, DoS analysis enables us to clearly identify those pores where saturated flow certainly occurs, i.e., pores with a DoS of 100% are
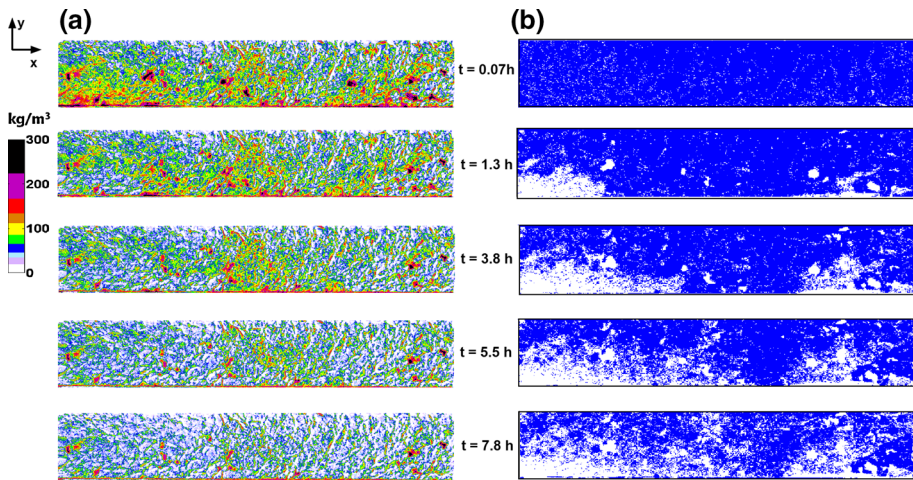
Fig. 9 Temporal evolution of **a** moisture content distribution and **b** the corresponding thresholded images in which *white pixels* represent a moisture loss of more than $30\,\text{kg/m}^3$ as compared to the wet image at $t = 90\,\text{s}$. The specimen is PA8(A), which was taped at the bottom, and the fan was switched on at $t = 1.2\,\text{h}$

certainly saturated with water. For pores that show a DoS of less than 100%, further analysis is required to distinguish between saturated and unsaturated flow.

Figure 10 shows the degree of saturation images for a region of interest of $30\,\text{mm} \times 15\,\text{mm}$ in the lower left corner of specimen PA8(A). The spatial distribution of DoS is given in Fig. 10a while the corresponding thresholded images, in which white pixels represent a reduction of more than 10% DoS compared to the wet image at $t = 90\,\text{s}$, are given in Fig. 10b. The total duration of the sudden moisture drop event analyzed here is less than 3 min and has been captured by six successive images of the RoI with a gap of 30 s between them. In Fig. 10b, the movement of the air front from left to right is clearly visible. From Fig. 10a, it can be seen that the color of most of the pixels in the middle region of the RoI change from green (20–30%) to blue (5–20%) as we go from $t = 33.5\,\text{min}$ to $t = 36\,\text{min}$. In the upper right corner, i.e., between $y = 10$ to $y = 15\,\text{mm}$ and $x = 18$ to $x = 25\,\text{mm}$, the reduction in DoS is much higher since the color changes from red to green. The highest reduction in DoS is at the bottom part of the RoI (which is also the bottom part of the specimen) where there is a connected region of fully saturated (black) pores at $t = 33.5\,\text{min}$. This black region almost completely disappears by $t = 36\,\text{min}$. Furthermore, the water front stops at $x = 30\,\text{mm}$ because it has reached a dead-end pore, as will be shown further. From these observations, there is a strong indication of a connected pore network which starts at $x = 30\,\text{mm}$ and ends at $x = 0$, where it is connected to the environment. The next step is to visualize this pore space from the X-ray μ-CT scans of the specimen.

In Fig. 11, the path followed by the draining water front, as opposed to the air front which was visualized in 2D in Fig. 10b, is now visualized in 3D within the actual three-dimensional geometry of the RoI. The predicted water path is shown by highlighting the pore cross section in black. The 3D image analysis software Avizo Fire 8.0 is used for this analysis. First, the three-dimensional volume of the specimen is rendered from the X-ray μ-CT images. Then, this volume is segmented into pores and non-pores (binders or aggregates). In the final step, all those pores which are not connected to the network under investigation are removed from the domain for the sake of clarity.
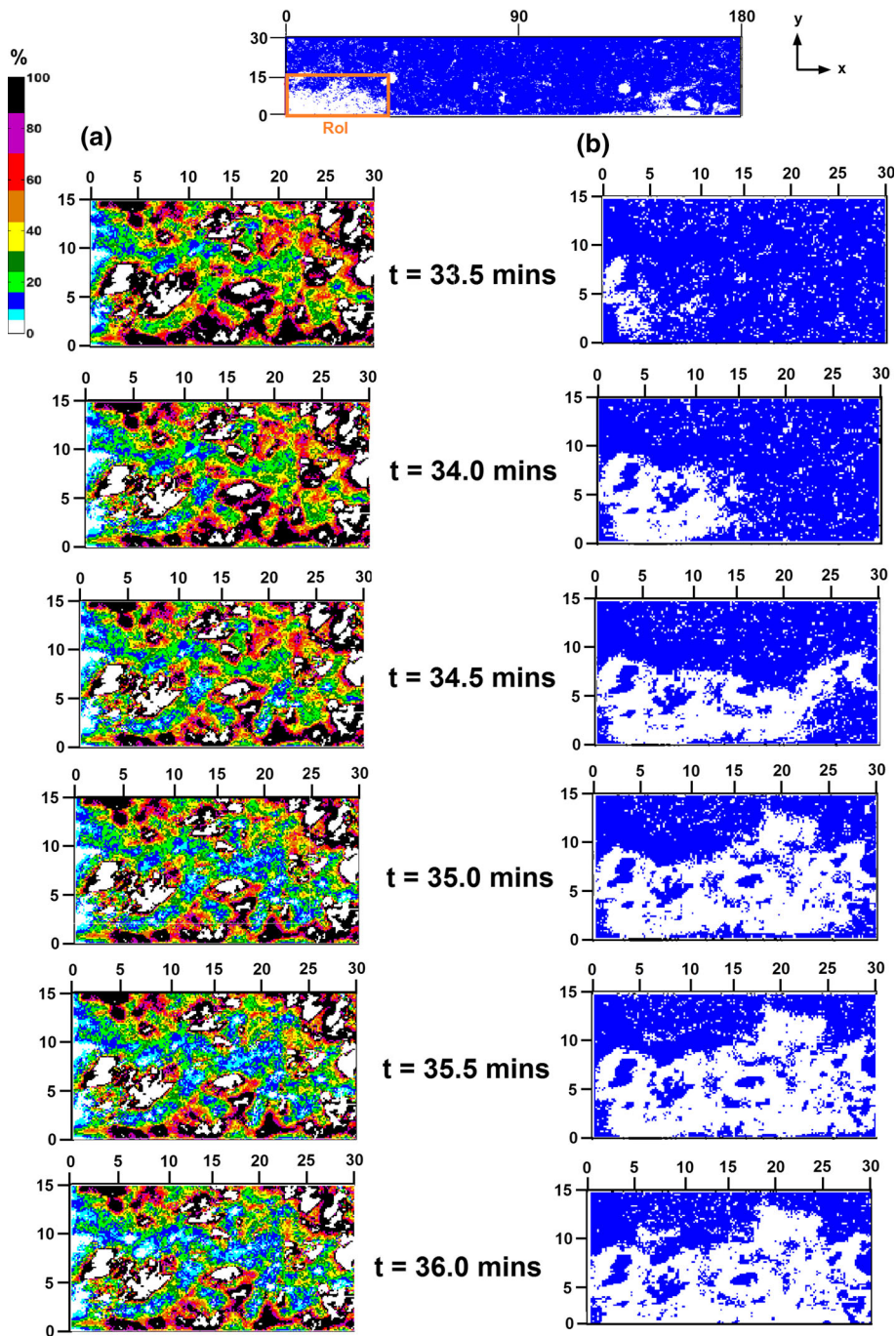
Fig. 10 **a** Degree of saturation images (DoS) and **b** the corresponding thresholded images (*right*) in which blue pixels represent a reduction of more than 10% degree of saturation as compared to the wet image at $t = 90$ s. The figures are for a region of interest (RoI) within the specimen PA8(A) where a sudden drop in moisture content occurs. All dimensions are in mm
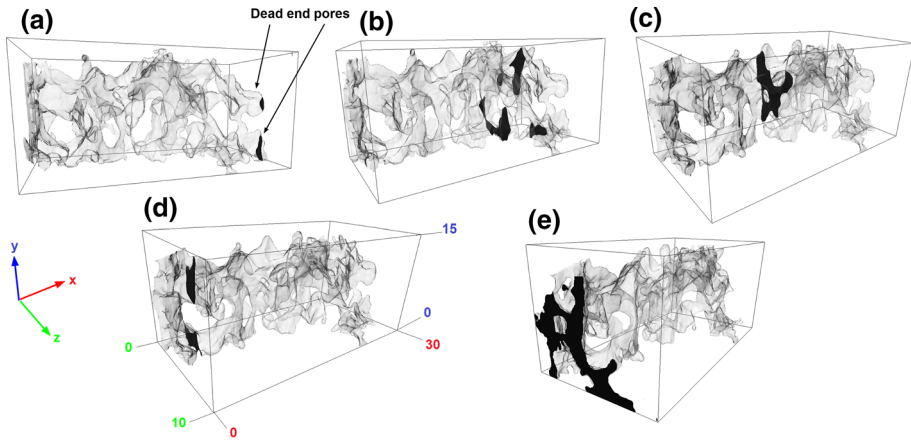
Fig. 11 Predicted path of the water front during the sudden drop in moisture content in PA8(A), between the time steps $t = 33.5$ min and $t = 36.0$ min, is shown in *black*. The pore geometry is obtained from 3D X-ray μ-CT scans and only the connected pores within the region of interest chosen in Fig. 10 are shown. The movement of water starts from the two dead-end pores shown in (**a**) and continues until the plane $x = 0$ (**e**), where it exits to the surroundings. Figures **b–d** show the likely water path from **a–e**. All dimensions are in mm

In Fig. 11, the movement of water occurring in the pore space starting from right to left is shown in black. Water starts moving from the two dead-end pores shown in Fig. 11a. From there, water continues to travel along the x-axis from $x = 30$ mm toward $x = 0$, where it finally exits from the specimen, as shown in Fig. 11e. At the plane $x = 0$, a large cross section of the pore network is exposed to the surrounding environment. The phenomenon seen here is analogous to the air entry point in soil hydrology, which is the water content at which air starts to penetrate the saturated porous medium (Braudeau et al. 1999). Once this water content is reached, the capillary pressure inside the specimen will be large enough to allow displacement of water by the invading air phase. This point is characterized by a sudden decline in water content, which is precisely what we observe in PA8(A) in Fig. 8d. Alternatively, this moisture drop could also be a "Haines jump" (Haines 1930). According to this theory, when a non-wetting phase (air) displaces a wetting phase (water), a situation is reached when the water meniscus can no longer increase its curvature at the narrowest pore of the air-water interface to cope up with the increasing capillary pressure. At this stage, the meniscus simply jumps to the next narrow capillary pore, thereby emptying the former pore instantaneously. Due to the favorable conditions for air entry at $x = 0$, and the presence of coarse pores that are connected to the internal structure of the specimen, a sudden drop in water content was seen in the RoI. The displacement of water by air cannot go further than $x = 30$ mm since at this point, the pore network reaches a dead end. It can also be observed that the direction of water propagation is not always directly in the direction of gravity. Drainage in PA8(A) through side pores, i.e., pores connected to the lateral edges of RoI 3, contributes to the high total moisture loss even though the bottom was taped, as was observed in Fig. 8d.

3.4 Analysis of Water Flow During Redistribution of Water Between Two Pores

Redistribution of water within the internal structure of PA, through capillary action and gravity, can have important consequences from the point of view of material durability.
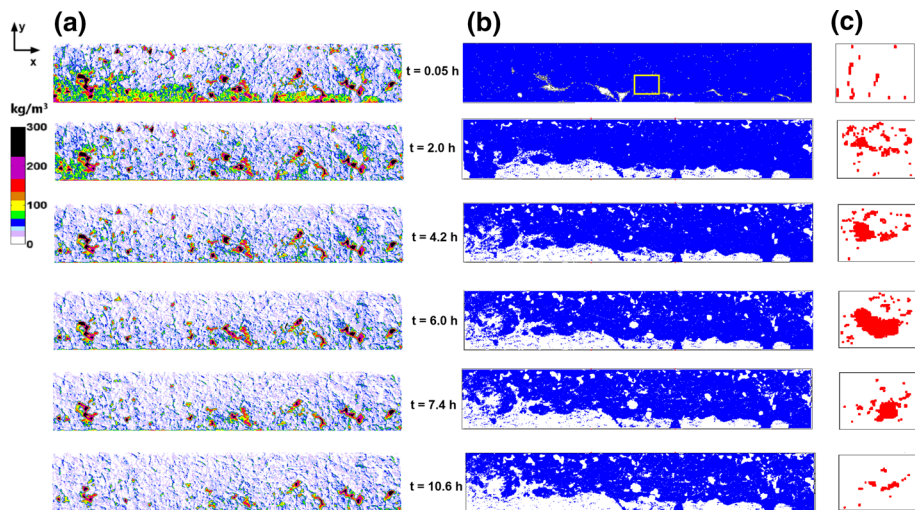
Fig. 12 Temporal evolution of **a** moisture content distribution, **b** the corresponding thresholded images in which blue pixels represent a moisture loss of more than $30\,kg/m^3$ as compared to the wet image at $t = 90\,s$ and **c** the thresholded images of a region of interest of $90 \times 67\,mm^2$, as shown with a *yellow box* in (**b**), in which *red pixels* represent a moisture gain of more than $20\,kg/m^3$ when compared to the wet image at $t = 90\,s$. The specimen is PA8(C), which was untaped at the bottom, and the fan was switched on at $t = 2\,h$

Redistribution of water can lead to the formation of disconnected water islands within the porous material, which can take a long time to drain or dry by evaporation. This leads to long periods of binder exposure to moisture, potentially affecting the mechanical properties of the binder in the long run. During the drainage/drying experiment of PA8(C), redistribution of water within the specimen was observed and is analyzed in detail in this section.

Figure 12a shows the spatial distribution of moisture content (in kg/m^3) in PA8(C) while Fig. 12b shows the corresponding thresholded images where a white pixel represents a moisture loss of more than $30\,kg/m^3$ as compared to the first wet image at $t = 90\,s$. In Fig. 12c, an additional column presents thresholded images of a region of interest of dimensions $90 \times 67\,mm^2$, marked in yellow in Fig. 12b, but with the important difference that the thresholding is performed for moisture gain, as opposed to moisture loss, when compared to the image at $t = 90\,s$. In Fig. 12c, a red pixel represents a moisture gain of more than $20\,kg/m^3$ when compared to the wet image at $t = 90\,s$ while a white pixel represents either no moisture gain or a moisture gain below the threshold of $20\,kg/m^3$. In a drying/drainage experiment, the only source of moisture gain within the specimen is water that is redistributed from other regions. Indeed, at $t = 6\,h$, a small region where moisture gain occurs can be observed. This region will be analyzed in detail in the subsequent paragraphs. When compared to the specimen PA8(A) in Fig. 9a, water retention is seen to be much lower in the specimen PA8(C) in Fig. 12a. This is expected since gravity-driven drainage is not constrained by a tape at the bottom of PA8(C). This is also the reason why there is a much larger difference in the moisture content distribution between the first two time steps in Fig. 12a as compared to the ones in Fig. 9a. Similar to PA8(A), a strong bottom-up air front movement can be observed in PA8(C). However, the bottom-up air front in PA8(C) is more distinctive since most of the water is exiting from the pores that are connected to the bottom plane, unlike in PA8(A) where water was blocked from exiting from the bottom side and consequently was exiting from the pores open to the lateral sides. Another important result from Fig. 12a is that a higher
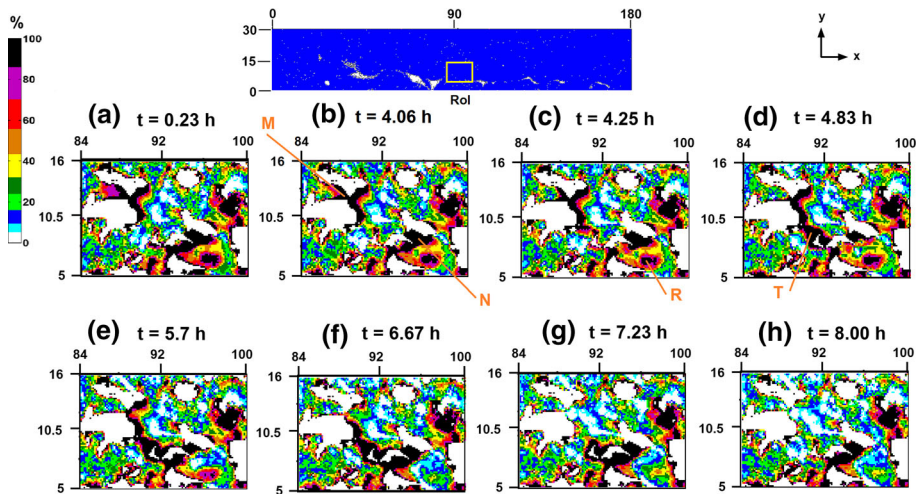
Fig. 13 Degree of saturation images of a region of interest within specimen PA8(C) where redistribution of water is observed. Water distribution takes place from pore A to pore B through throat T. Pore B is in turn connected to a reservoir R. All dimensions are in mm

moisture retention at the lower part of the specimen, which is the reason for the observations made from Figs. 6 and 7, is clearly observed at $t = 0.05$ h. Furthermore, as mentioned in the discussion of Fig. 6, the large cluster of water which is present at the bottom left corner of PA8(C) at $t = 2$ h is significantly smaller at $t = 4.2$ h. This accounts for the sharp change of slope in the moisture content of PA8(C) between the same time steps in Fig. 6.

We now analyze in more detail the redistribution of water within PA8(C) observed in Fig. 12c by looking at the degree of saturation images for a RoI of 16×11 mm^2 in Fig. 13. A fully saturated region (black) which moves from the upper left corner to the lower right corner of the RoI can be clearly seen. This redistribution of water takes place over 4 h, indicating a slow process. At $t = 4.06$ h, there is a quasi-stable configuration of a connected water phase stretching from a fully saturated pore in the upper left corner ($x = 86$ to $x = 90$ mm and $y = 10$ to $y = 14$ mm), named pore M, to a fully saturated pore in the lower right corner ($x = 92$ to $x = 96$ mm and $y = 6$ to $y = 10$ mm), named pore N, as marked in Fig. 13b. These two pores are connected by a throat, throat T, which is marked in Fig. 13d. At $t = 4.06$ h, throat T is not completely filled. Therefore, an unsaturated capillary flow like film or corner flow could be present inside the throat. Pore N is connected to a reservoir, reservoir R, marked in Fig. 13c. The trigger for the redistribution of water from pores M to N is the drainage of reservoir R, which begins at $t = 4.06$ h. As the drainage of R begins, the water saturation level of N decreases, which triggers the redistribution of water from M to N through T. During this redistribution process, T is fully saturated with water, as can be seen in Fig. 13d–f. The redistribution of water finally ends when most of the water in R is drained by $t = 8$ h, as seen in Fig. 13h.

In Fig. 14, using the methods used earlier for obtaining Fig. 11, we present the 3D reconstruction of the RoI analyzed in Fig. 13, where water redistribution was observed. The pores M and N as well as throat T, which are distinctly marked in Fig. 13, can be clearly visualized in Fig. 14. Reservoir R was not clearly distinguishable from the X-ray μ-CT scans, and hence, it is not presented here. The predicted water path is shown by highlighting the pore cross section in black. The redistribution of water from pore M to pore N through throat
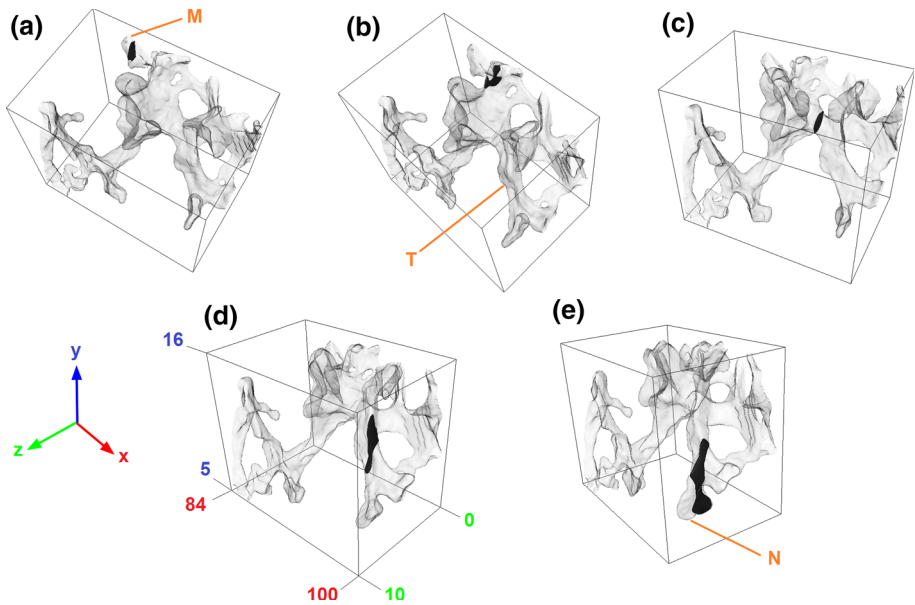
Fig. 14 Path of water redistribution within PA8(C), between the time steps $t = 4.06$ h and $t = 8$ h, is shown in black. The pore geometry is obtained from 3D X-ray μ-CT scans and only the connected pores within the region of interest chosen in Fig. 11 are shown. Water travels from pore M to pore N through throat T. All dimensions are in mm

T is visualized in Fig. 14. Moreover, Fig. 14 also illustrates the wide range of connectivity numbers in a typical PA pore network. Connectivity (also called coordination number) is defined as the number of pores connected to a given pore and can be calculated from a binary image after pore segmentation. In this small segment itself, connectivity numbers ranging from 1 to 5 can be observed. For future pore network simulations of water transport inside PA, information about connectivity numbers from such 3D visualizations will be an important input parameter.

The in-depth analysis presented in this section illustrates the complex nature of water movement in porous asphalt, a macroporous medium. On the one hand, gravity-driven drainage causes sudden drops in moisture content in one specimen while, on the other hand, we observe a slow redistribution of water within another specimen. The simultaneous prevalence of gravity-driven drainage in large pores and capillary-driven movement of water in smaller pores is unique to a material like porous asphalt due to its wide range of pore sizes. Additionally, local surface roughness, hydrophobicity of the solid (bitumen or aggregate) in contact with water, tortuosity of the pore network, etc., can influence the water flow inside PA. Experimental studies like the ones reported in this study can give an insight into the relative importance of each of these parameters in determining the residence time of water inside the specimen. Moreover, a clear pattern of water flow like the redistribution between pores as observed in this study can serve as validation for multiphase flow simulations. From the results reported in this study, it is clear that gravity-driven drainage is the most important factor responsible for the overall moisture loss from a wet PA specimen. The influence of possible air penetration into the structure at higher wind speeds and the exact type of wetting (discrete or continuous) on the drying rate will be investigated in future experiments.

4 Conclusions

Drainage and forced convective drying in porous asphalt, a macroporous media, are studied using neutron radiography (NR) in a custom-made mini wind tunnel. Three specimens of two types of porous asphalt are used in the experiments, of which one type has larger aggregate sizes and consequently larger pore sizes. The specimens are fully saturated at the beginning of the experiments. Gravity-driven drainage is constrained in the vertical direction in two of the specimens to observe its effect on the overall moisture loss. By combining neutron radiography and microcomputer tomography, saturation degree distributions are obtained, from which the regions where saturated flow is active can be identified. Based on the experimental results, the following important observations and conclusions are made:

1. In all specimens, maximum water retention is at the bottom region of the specimens due to strong influence of gravity-driven drainage in the higher regions. As a result, most of the moisture loss is from the bottom region, despite the larger diffusion lengths of the water vapor generated from the bottom region. The drying or drainage of large clusters of water close to an open edge result in bursts of moisture content decrease.
2. The effect of airflow on the drying rate is different in the taped and untaped specimens. In the taped specimens, a higher accumulation of moisture in the top region of the specimen leads to lower vapor diffusion lengths, and therefore faster drying on the introduction of airflow.
3. Even after many hours of forced convective drying, water retention can be seen inside the specimens, which points to the strong resistance to evaporation in PA as a result of the large vapor diffusion lengths.
4. In one of the specimens in which gravity-driven drainage at the bottom was constrained, a sudden drop in moisture content is attributed to air invasion in a pore that was connected to the lateral edge. The air front proceeded until it is stopped by reaching dead-end pores.
5. Water redistribution between two pores is clearly observed. The total duration of this redistribution is close to four hours. Water moved from one pore to another by saturated flow through the throat which connected the two pores.
6. Both the observed phenomena, i.e., sudden drop in moisture content and water redistribution, are visualized by reconstructing the actual three-dimensional pore geometry from X-ray µ-CT scans.

The fact that even after many hours of drainage and drying, water is still retained in the material is an indication of the importance of choosing PA materials that are not (or are less) water sensitive and to develop means to reduce the water sensitivity of such materials. The influence of other environmental factors besides wind, such as solar radiation, discrete droplet wetting will be analyzed in a future paper.

References

Aboufoul, M., Garcia, A.: Factors affecting hydraulic conductivity of asphalt mixture. Mater. Struct. **50**(2), 116 (2017). doi:10.1617/s11527-016-0982-6

Alvarez, G., Flick, D.: Modelling turbulent flow and heat transfer using macro-porous media approach used to predict cooling kinetics of stack of food products. J. Food Eng. **80**, 391–401 (2007)

Amiri, A., Vafai, K., Kuzay, T.M.: Effects of boundary conditions on non-Darcian heat transfer through porous media and experimental comparisons. Numer. Heat Transf. Part A: Appl. **27**(6), 651–664 (1995)

Bergstad, M., Shokri, N.: Evaporation of NaCl solution from porous media with mixed wettability. Geophys. Res. Lett. **43**(9), 4426–4432 (2016)

Braudeau, E., et al.: New device and method for soil shrinkage curve measurement and characterization. Soil Sci. Soc. Am. J. **63**, 525–535 (1999)

Calmidi, V.V., Mahajan, R.L.: Forced convection in high porosity metal foams. J. Heat Transf. **122**, 557–565 (2000)

Cui, Y.-J., Zornberg, J.G.: Water balance and evapotranspiration monitoring in geotechnical and geoenvironmental engineering. Geotech. Geol. Eng. **26**(6), 783–898 (2008). doi:10.1007/s10706-008-9198-z

Defraeye, T., Blocken, B., Carmeliet, J.: Analysis of convective heat and mass transfer coefficients for convective drying of a porous flat plate by conjugate modelling. Int. J. Heat Mass Transf. **55**, 112–124 (2012). doi:10.1016/j.ijheatmasstransfer.2011.08.047

Dong, H., Blunt, M.: Pore-network extraction from micro-computerized-tomography images. Phys. Rev. E **80**(3), 36307 (2009). doi:10.1103/PhysRevE.80.036307. (Accessed September 3, 2014)

Feldkamp, L.A., Davis, L.C., Kress, J.W.: Practical cone-beam algorithm. J. Opt. Soc. Am. A **1**(6), 612–619 (1984)

Fenwick, D.H., Blunt, M.J.: Three-dimensional modeling of three phase imbibition and drainage. Adv. Water Resour. **21**(2), 121–143 (1998)

Geller, J.T., Hunt, J.R.: Mass transfer from nonaqueous phase organic liquids in water-saturated porous media. Water Resour. Res. **29**(4), 833–845 (1993)

van Genuchten, M.T., Wierenga, P.J.: Mass transfer studies in sorbing porous media: II. Experimental evaluation with tritium (3H2O)1. Soil Sci. Soc. Am. J. **41**, 272–278 (1977)

Gostick, J.T., et al.: Pore network modeling of fibrous gas diffusion layers for polymer electrolyte membrane fuel cells. J. Power Sources **173**(1), 277–290 (2007)

Grattoni, C.A., Jing, X.D., Dawe, R.A.: Dimensionless groups for three-phase gravity drainage flow in porous media. J. Pet. Sci. Eng. **29**, 53–65 (2001)

Haghighi, E., et al.: Evaporation rates across a convective air boundary layer are dominated by diffusion. Water Resour. Res. **49**(3), 1602–1610 (2013)

Haines, W.B.: Studies in the physical properties of soil. V. The hysteresis effect in capillary properties, and the modes of moisture distribution associated therewith. J. Agric. Sci. **20**(1), 97–116 (1930)

Hassanein, R., Lehmann, E., Vontobel, P.: Methods of scattering corrections for quantitative neutron radiography. Nucl. Instrum. Methods Phys. Res. Sect. A: Accel. Spectrom. Detect. Assoc. Equip. **542**, 353–360 (2005)

Hillel, D.: Soil and Water. Physical Principles and Processes. Academic Press, New York (1971)

Hirsch, L.M., Thompson, A.H.: Size-dependent scaling of capillary invasion including buoyancy and pore size distribution effects. Phys. Rev. E **50**(3), 2069–2086 (1994). doi:10.1103/PhysRevE.50.2069

Hoogland, F., Lehmann, P., Or, D.: Drainage dynamics controlled by corner flow: application of the foamdrainage equation. Water Resour. Res. **52**, 8402–8412 (2016)

James, C., et al.: Numerical and experimental data set for benchmarking hygroscopic buffering models. Int. J. Heat Mass Transf. **53**(19–20), 3638–3654 (2010). doi:10.1016/j.ijheatmasstransfer.2010.03.039

Kuznetsov, A.V., Nield, D.A.: Thermally developing forced convection in a bidisperse porous medium. J. Porous Media **9**(5), 393–402 (2006)

Lal, S., et al.: Investigation of Water Uptake in Porous Asphalt Concrete Using Neutron Radiography. Transport in Porous Media. **105**(431–450), 2014 (2014). doi:10.1007/s11242-014-0376-6. Accessed October 13

Lehmann, E.H., Vontobel, P., Wiezel, L.: Properties of the radiography facility NEUTRA at SINQ and its potential for use as European reference facility. Nondestruct. Test. Evaluat. **16**, 191–202 (2001)

Moghaddam, A.A., et al.: Kinematics in a slowly drying porous medium: reconciliation of pore network simulations and continuum modeling. Phys. Fluids. **29**, 022102 (2017). doi:10.1063/1.4975985

Moghaddam, M.B., Rasaei, M.R.: Experimental Study of the Fracture and Matrix Effects on Free-Fall Gravity Drainage With Micromodels. SPE J., **20**(2), 324–336 (2015). https://www.onepetro.org/journal-paper/SPE-171555-PA. Accessed 9 Feb 2016

Partl, M.N., et al.: Characterization of water sensitivity of asphalt mixtures with coaxial shear test. Road Mater. Pavement Des., **9**(2), pp. 247–270 (2008). http://www.scopus.com/inward/record.url?eid=2-s2.0-47249155265&partnerID=tZOtx3y1

Poulikakos, L.D., et al.: Forced convective drying of wet porous asphalt imaged with neutron radiography. Adv. Eng. Mater., **15**(11), 1136–1145 (2013). doi:10.1002/adem.201300027. Accessed 13 Oct 2014

Poulikakos, L.D., et al.: Time resolved analysis of water drainage in porous asphalt concrete using neutron radiography. Appl. Radiat. Isotopes, **77**, 5–13 (2013). http://www.ncbi.nlm.nih.gov/pubmed/23500651. Accessed 13 Oct 2014

Poulikakos, L.D., Partl, M.N.: A multi-scale fundamental investigation of moisture induced deterioration of porous asphalt concrete. Construct. Build. Mater., **36**, pp. 1025–1035 (2012). http://linkinghub.elsevier.com/retrieve/pii/S0950061812002735. Accessed 17 Oct 2014

Poulikakos, L.D., Partl, M.N.: Investigation of porous asphalt microstructure using optical and electron microscopy. J. Microsc. **240**(March), 145–154 (2010)

Prazak, J., et al.: Oscillation phenomena in gravity-driven drainage in coarse porous media. Water Resour. Res. **28**(7), 1849–1855 (1992)

Shokri, N., Sahimi, M., Or, D.: Morphology, propagation dynamics and scaling characteristics of drying fronts in porous media. Geophys. Res. Lett. **39**(9), 1–5 (2012)

Teng, Y., et al.: A visualization study on two-phase gravity drainage in porous media by using magnetic resonance imaging. Magnetic Reson. Imag. **34**(7), 855–863 (2016). doi:10.1016/j.mri.2016.03.004

Vafai, K.: Convective flow and heat transfer in variable-porosity media. J. Fluid Mech., **147**, 233–259 (1984). http://www.journals.cambridge.org/abstract_S002211208400207X

Vafai, K., Alkire, R.L., Tien, C.L.: An experimental investigation of heat transfer in variable porosity media. Trans. ASME **107**, 642–647 (1985)

Watts, G.R., Chandler-Wilde, S.N.: Morgan, Pa: The combined effects of porous asphalt surfacing and barriers on traffic noise. Appl. Acoust. **58**, 351–377 (1999)

Yang, M., Yanful, E.K.: Water balance during evaporation and drainage in cover soils under different water table conditions. Adv. Environ. Res. **6**(4), 505–521 (2002)